Tunable topological bandgaps and frequencies in a pre-stressed soft phononic crystal

Cite as: J. Appl. Phys. **125**, 095106 (2019); https://doi.org/10.1063/1.5066088
Submitted: 12 October 2018 . Accepted: 04 February 2019 . Published Online: 06 March 2019

B. H. Nguyen, X. Zhuang, H. S. Park, and T. Rabczuk

Journal of Applied Physics ARTICLE scitation.org/journal/jap

Tunable topological bandgaps and frequencies in a pre-stressed soft phononic crystal

Cite as: J. Appl. Phys. **125**, 095106 (2019); doi: 10.1063/1.5066088
Submitted: 12 October 2018 · Accepted: 4 February 2019 ·
Published Online: 6 March 2019

B. H. Nguyen,[1,2] X. Zhuang,[1,3,a)] H. S. Park,[4] and T. Rabczuk[5]

AFFILIATIONS

[1]Division of Computational Mechanics, Ton Duc Thang University, Ho Chi Minh City, Vietnam
[2]Institute of Continuum Mechanics, Leibniz University Hanover, Hanover, Germany
[3]Faculty of Civil Engineering, Ton Duc Thang University, Ho Chi Minh City, Vietnam
[4]Department of Mechanical Engineering, Boston University, Boston, Massachusetts 02215, USA
[5]Institute of Structural Mechanics, Bauhaus-Universität Weimar, Weimar, Germany

[a)]**Author to whom correspondence should be addressed:** xiaoying.zhuang@tdtu.edu.vn

ABSTRACT

Topological insulators (TIs) have recently received significant attention due to the promise of lossless transport of various types of energy. Despite this interest, one outstanding issue is that the topological bandgap and the frequencies that are topologically permitted are typically fixed once the topological structure has been designed and fabricated. Therefore, an open and unresolved question concerns the ability to actively tune both the bandgap magnitude, as well as the frequencies, for which the energy is topologically protected. In this work, we report a mechanically tunable phononic TI using an acoustic analog of the quantum valley Hall effect. We propose a phononic crystal comprised of a soft, hyperelastic material where the phononic band structure is modulated through large deformation of the structure. In doing so, space-inversion symmetry can be broken, which leads to a phase transition between two topologically-contrasted states and the emergence of topologically-protected interface modes according to bulk-edge correspondence. We further demonstrate the robustness of this topological protection of the edge state along the interface, which demonstrates that mechanical deformation can be used to effectively tailor and tune the topological properties of elastic structures.

I. INTRODUCTION

Topological insulators (TIs) have received significant interest since their discovery more than a decade ago. A primary reason for this interest is because of the potential for lossless guiding and directing of waves of various types.[1] While originally discovered in quantum electronic systems, acoustic analogs of the electronic system have recently been devised to exploit this unique edge state property. Some early attempts were based on the quantum Hall effect (QHE), in which the time reversal symmetry (TRS) is broken to obtain non-trivial Chern numbers by means of spinning rotors[2,3] or circulating fluids.[4] Other versions of acoustic TIs have been based on the quantum spin Hall effect (QSHE) where the TRS remains intact and the helical topologically-protected edge state is obtained by creating pseudo-spins.[5–8]

However, there are various challenges in realizing chiral (i.e., QHE-based) and helical (i.e., QSHE-based) topologically-protected edge states in acoustic systems. First, the breaking of TRS and space-inversion symmetry (SIS) depends on fully passive mechanisms[9–13] or involves complex rotating parts.[8,14] Furthermore, there are significant complications in designing QSHE-based TIs because of the need to generate a fourfold Dirac-like degeneracy in the band structure.[5]

Alternatively, there has been growing interest in quantum valley Hall effect (QVHE)-based TIs, which are significantly easier to design. In particular, many papers have reported variations in QVHE-based TIs in which SIS is broken in a hexagonal lattice structure in order to achieve twofold degeneracy in the band structure,[8,9,11,12,14–18] including recent works demonstrating such effects in two-dimensional nanostructures such as hexagonal boron nitride and silicon carbide.[19]

While the above details the various approaches to design acoustic TIs, one outstanding issue is that the topological bandgap and the frequencies that are topologically permitted

are typically fixed once the topological structure has been designed and fabricated. In contrast, there may be many applications in which it is desirable to be able to dynamically or adaptively tune the bandgap and the allowed frequencies after the structure has been fabricated. There have been several recent works addressing this issue. For example, Liu and Semperlotti[17,20] demonstrated the use of large displacements in truss-like structures to design a tunable acoustic valley-Hall edge state. Similarly, Susstrunk *et al.*[21] utilized local symmetry breaking potentials to design a switchable topological phonon channel.

In this work, we propose a strain-driven mechanism that utilizes the large, nonlinear deformation of a soft material to break SIS of a hexagonal lattice and design a QVHE-based phononic TI. We demonstrate that both the bandgap and the frequency are highly tunable using reasonable amounts of mechanical stress. The remainder of the paper is as follows: in Sec. II, we summarize the deformation of the soft annulus. The incremental equation of motion is derived with respect to the deformed state, from which Bloch's theorem and the finite element method (FEM) are employed to obtain the phononic band structure. By analyzing the dispersion relation, the topological invariant valley Chern number is calculated, which indicates the number of interface modes between two contrasting topological structures. In Sec. III, we verify the existence of this interface mode in a finite super-cell. Existence of this interface mode enables robust one-way wave propagation in a phononic metamaterial as will be demonstrated in Sec. IV. Conclusions are given in Sec. V.

II. TUNABLE TOPOLOGICAL BAND-STRUCTURE

A. Problem description

The geometry we consider in this work is an isotropic, incompressible hyperelastic cylindrical annulus with inner radius R_0 and outer radius R_1 of density ρ_1, shear modulus μ_1

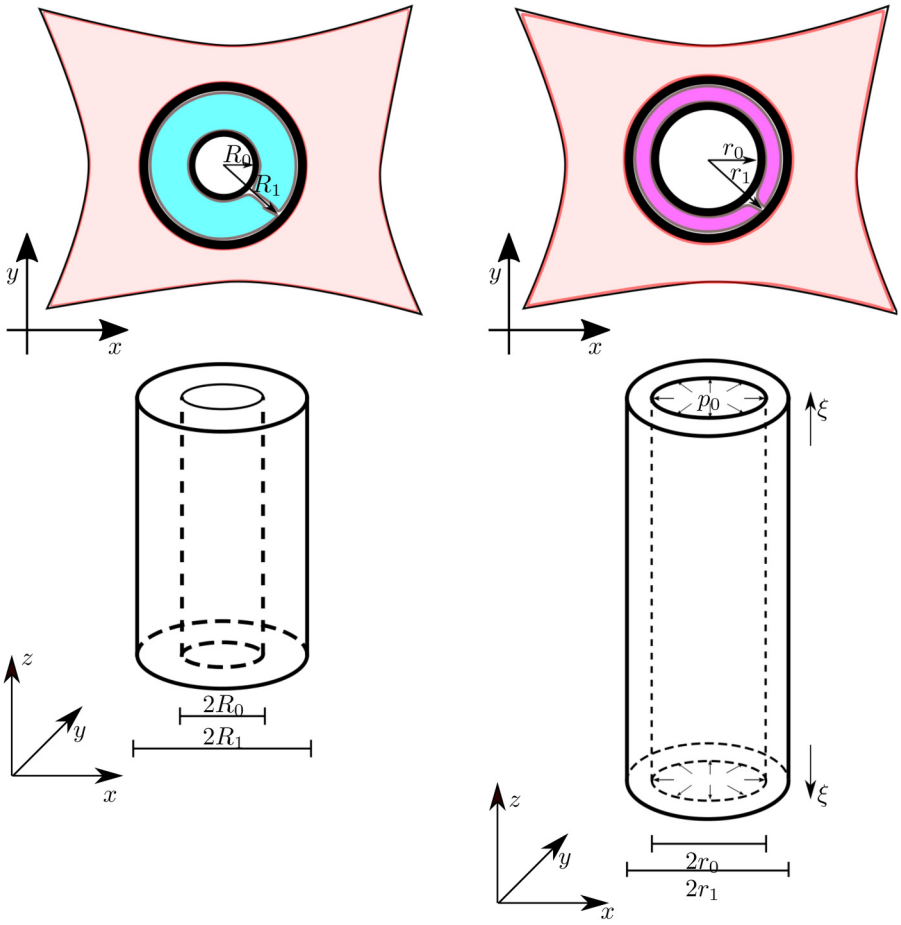

FIG. 1. The inflation of a hyperelastic cylindrical annulus embedded in an elastic medium and subjected to internal pressure p_0 and longitudinal stretch (adapted from Ref. 22). The inflation could be realized in practice by increasing the pressure inside the annulus through internal fluid pressure or an inviscid gas.[23,24] The initial inner and outer radii of the cylindrical annulus are R_0 and R_1, whereas those of the deformed one are r_0 and r_1, such that $r_1 = R_1$ by appropriate choice of stretch value ξ.

embedded into a linear elastic host medium of density ρ_0, and shear modulus μ_0 as depicted in Fig. 1. This geometry is motivated by the recent work of Barnwell[22] and Barnwell *et al.*[23] Specifically, the cylindrical annulus is inflated by applying an internal pressure on the inner surface and axial stretch ξ in such a manner that the outer radius R_1 is remained unchanged as schematically shown in Fig. 1. The inflation could be realized in practice by increasing the pressure inside the annulus through internal fluid pressure or an inviscid gas.[23,24] As also noted in Ref. 24, the magnitude of the internal pressure p_0 that is needed in order to expand the ring 20 times than its original size can be estimated as $p_0/\mu \approx 3.5$, where the shear modulus μ for rubber for a Neo-Hookean material is $\mathcal{O}(10^5)\,Pa$. In the cylindrical coordinate system, where the origin is the center of the annulus, the inflation of the cylindrical annulus is described by expressing the coordinates in the reference configuration in terms of those in the current configuration such as

$$R = R(r), \quad \Theta = \theta, \quad Z = \frac{z}{\xi}, \tag{1}$$

where the upper case and lower case convention is used to denote the reference and current configuration, respectively. Consequently, by forming the deformation gradient and utilizing the spectral decomposition, the principal stretches can be obtained as

$$\lambda_r = \frac{1}{R'(r)}, \quad \lambda_\theta = \frac{r}{R(r)}, \quad \lambda_z = \xi. \tag{2}$$

Because we focus on using soft, hyperelastic materials for the annulus, the radial displacement function $R(r)$ is now determined by using the incompressibility condition, i.e., $\lambda_r\lambda_\theta\lambda_z = 1$ and the boundary condition such that

$$R_0 = R(r_0), \quad R_1 = R(r_1) = r_1, \tag{3}$$

which then results in

$$R(r) = \sqrt{\xi\left[r^2 + \left(\frac{1}{\xi} - 1\right)R_1^2\right]}. \tag{4}$$

Furthermore, the radial Cauchy stress σ_{rr} due to the inflation of the annulus is given as[23]

$$\sigma_{rr}(r) = -p_0 + \int_{r_0}^{r_1} \frac{1}{s}\left[\lambda_\theta(s)\frac{\partial W}{\partial \lambda_\theta} - \lambda_r(s)\frac{\partial W}{\partial \lambda_r}\right] ds, \tag{5}$$

where W is the energy density function of the annulus, such that $\sigma_{rr}(r_0) = -p_0$ and $\sigma_{rr}(r_1) = 0$.

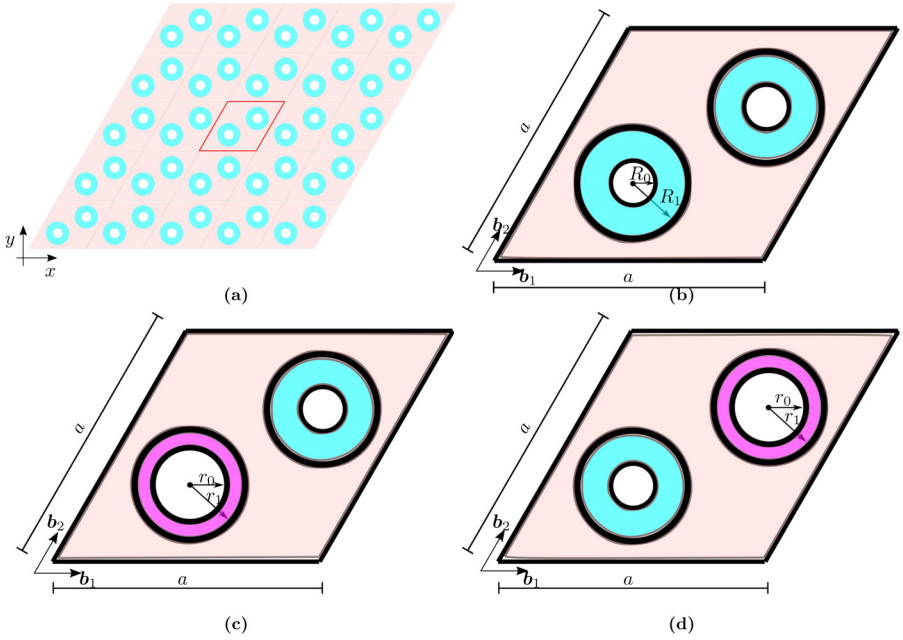

FIG. 2. Schematic of the PC and unit cells. (a) The PC consists of a hexagonal lattice where the soft annulus is embedded in an elastic medium. The initial radii are chosen as $R_0 = 0.05a$ and $R_1 = 0.2a$. (b) Unit cell of the unstrained annulus. (c) A-type unit cell when the lower annulus is inflated. (d) B-type unit cell when the upper annulus is inflated.

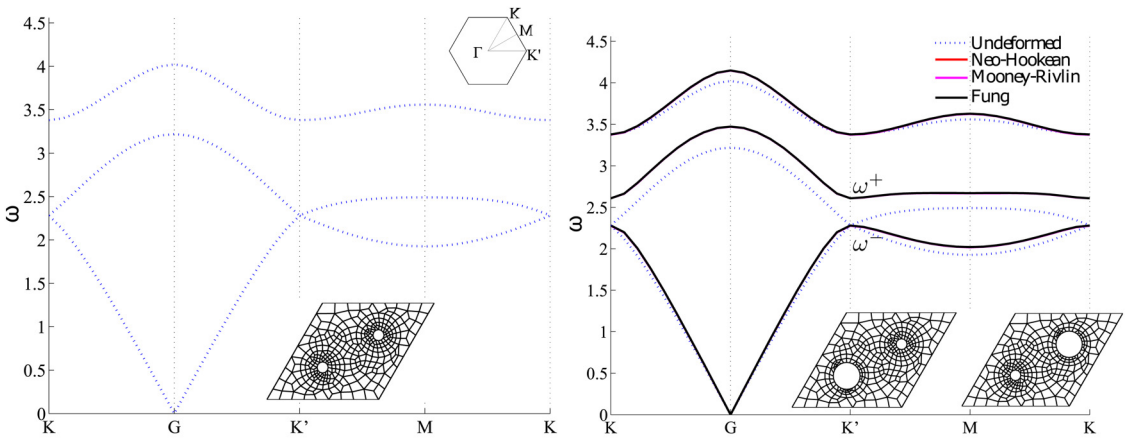

(a) Energy band diagram (b) Energy band diagram

FIG. 3. Phononic band diagram of (a) stress-free and (b) pre-stressed unit cells. Doubly degeneracy Dirac cone is observed at *K* and *K′* points when SIS is intact. The bandgap is opened when SIS is broken.

The above equations describe the static large deformation (or inflation) of the cylindrical annulus. On this deformed state, small-amplitude time-harmonic motions of the form $\exp(-i\omega t)$ with ω the angular frequency are prescribed. In order to describe the small-amplitude motion of a pre-stressed medium, the small-on-large theory is employed. Details of this theory can be found in Refs. 25 and 26 for general wave motion in solids. Nevertheless, in the context of this current work, we focus on antiplane waves polarized in the z-direction, of which the governing incremental equation is given as[23]

$$\frac{1}{r}\frac{\partial}{\partial r}\left[r\mu_r(r)\frac{\partial w}{\partial r}\right]+\frac{1}{r^2}\frac{\partial}{\partial \theta}\left[r\mu_\theta(r)\frac{\partial w}{\partial \theta}\right]+\rho\omega^2 w=0. \tag{6}$$

In the above equation, $\mu_r(r)$ and $\mu_\theta(r)$ are the incremental shear moduli, which are dependent on the

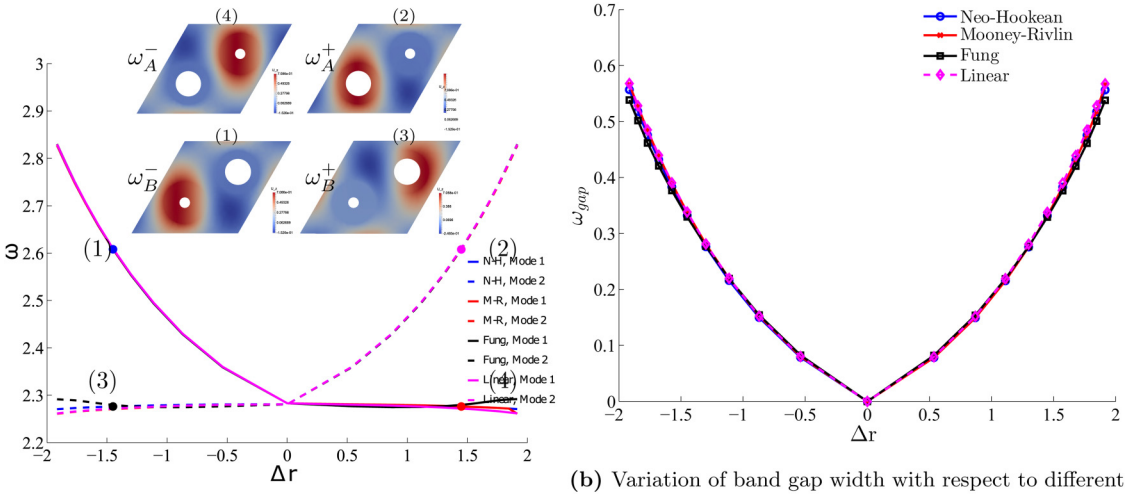

(a) Inversion of the first and second eigenmode. (b) Variation of band gap width with respect to different radii

FIG. 4. Stretch-based tunability demonstrates topological phase transition. (a) Variation of the eigenfrequency of the first two modes at *K* point. The insets show the corresponding eigenmodes of the A-type and B-type unit cell being stretched with $\xi = 1.5$ from the Neo-Hookean material. The eigenmodes are flipped across $\Delta r = 0$ (i.e., $\xi = 0$), indicating the occurrence of topological phase transition. (b) Variation of the bandgap width with respect to stretches.

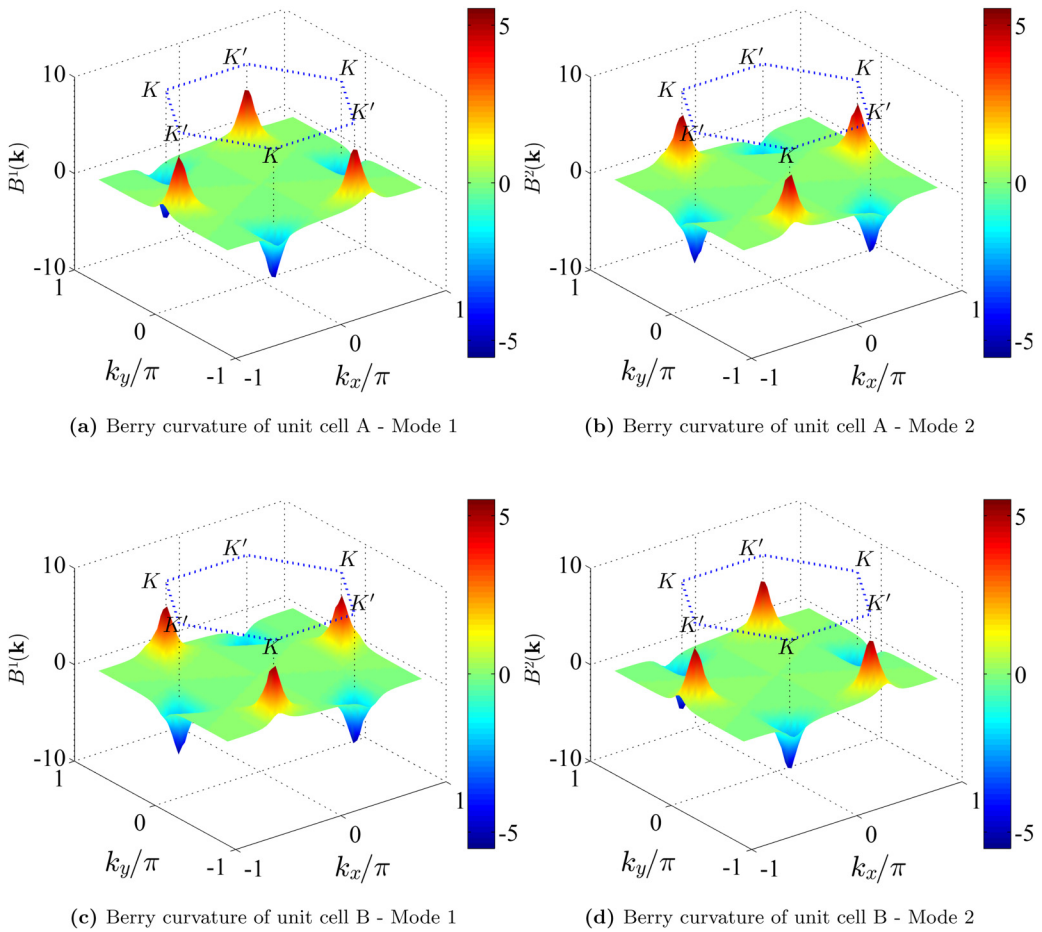

(a) Berry curvature of unit cell A - Mode 1 (b) Berry curvature of unit cell A - Mode 2

(c) Berry curvature of unit cell B - Mode 1 (d) Berry curvature of unit cell B - Mode 2

FIG. 5. Berry curvature of the first two eigenmodes of two types of unit cells. The Berry curvature is localized at K and K', having the same magnitude but different signs.

choice of the energy density function $W(\lambda_r, \lambda_\theta, \lambda_z)$ such that

$$\mu_r(r) = \left(\frac{\lambda_r \frac{\partial W}{\partial \lambda_r} - \lambda_z \frac{\partial W}{\partial \lambda_z}}{\lambda_r^2 - \lambda_z^2}\right)\lambda_r^2, \tag{7a}$$

$$\mu_\theta(r) = \left(\frac{\lambda_\theta \frac{\partial W}{\partial \lambda_\theta} - \lambda_z \frac{\partial W}{\partial \lambda_z}}{\lambda_\theta^2 - \lambda_z^2}\right)\lambda_\theta^2. \tag{7b}$$

In this current work, following the choice of the energy density function in Ref. 23, we also investigate three different material models, namely, the Neo-Hookean, the Mooney-Rivlin, and the Fung models, from which the incremental shear moduli can be determined analytically and are given in the Appendix.

Since the unit cell and the phononic structure (PC) are defined in the Cartesian coordinate system, the incremental wave equation (6) is now transformed back to the Cartesian coordinate system in terms of stresses such as

$$\nabla \cdot (\sigma_{zx} e_x + \sigma_{zy} e_y) + \rho\omega^2 w = 0, \tag{8}$$

where the shear stresses are given as

$$\sigma_{zx} = C_{zxzx}\frac{\partial w}{\partial x} + C_{zxzy}\frac{\partial w}{\partial y}, \tag{9a}$$

$$\sigma_{zy} = C_{zyzx}\frac{\partial w}{\partial x} + C_{zyzy}\frac{\partial w}{\partial y}, \tag{9b}$$

with

$$C_{zxzx} = \frac{1}{x^2 + y^2}(x^2\mu_r + y^2\mu_\theta), \tag{10a}$$

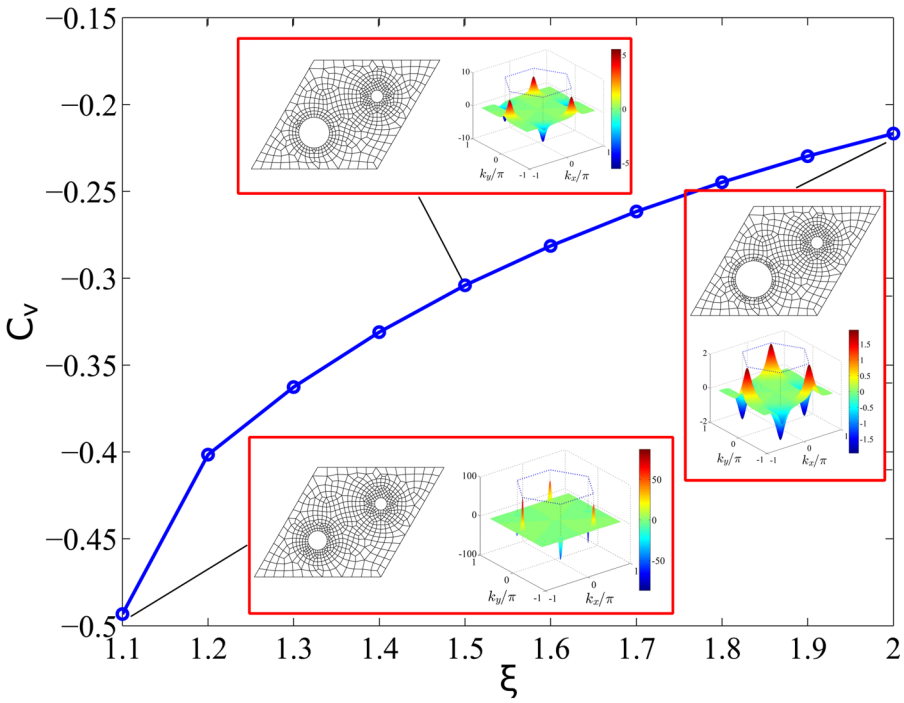

FIG. 6. Variation of the numerical valley Chern number C_v at the K-point of the first eigenmode of unit cell A, as a function of stretch ξ. The insets show the FEM mesh and Berry curvature at different ξ. The smaller the stretch ξ, i.e., the weaker the intensity of SIS breaking, the more localized the Berry curvature is at the Dirac points.

$$C_{zxzy} = C_{zyzx} = \frac{xy}{x^2+y^2}(\mu_r - \mu_\theta), \tag{10b}$$

$$C_{zyzy} = \frac{1}{x^2+y^2}(y^2\mu_r + x^2\mu_\theta). \tag{10c}$$

For numerical analysis, the material parameters are chosen as $\rho_0 = 1$, $\mu_0 = 1$ for the host medium, whereas those of the annulus are $\rho_1 = 2$, $\mu_1 = 50$.

B. Phononic band structure

The energy band structure of the phononic structure can be determined through a numerical solution of Eq. (8) by utilizing Bloch's theorem and the FEM to obtain the eigenvalue problem

$$[\mathbf{K}(\mathbf{k}) - \omega^2\mathbf{M}]\mathbf{w} = \mathbf{0}, \tag{11}$$

where $\mathbf{K}(\mathbf{k})$ and $\mathbf{M}$ are the stiffness and mass matrix that take into account the Bloch's theorem, $\mathbf{k}$ is the wavevector in the reciprocal space, and ω and $\mathbf{w}$ are, respectively, the eigenvalues and eigenmodes. The unit cell is discretized by 4-node bilinear quadrilateral finite elements as shown in the insets of Fig. 3, in order to obtain the stiffness and mass matrices that are given in the Appendix. The resulting phononic crystal is a hexagonal lattice with lattice constant $a = 1$ that consists of a hyperelastic annulus embedded in a linear elastic medium (as described in Sec. II A) and is schematically depicted in Fig. 2(a). The unit cell is chosen as in Fig. 2(b) and is comprised of two annuli. In the initial (undeformed) configuration, the unit cell supports $C3v$ symmetry such that the Dirac point between the first two eigenmodes can be obtained at the K and K' points in the reciprocal space as shown in Fig. 3(a). Subsequently, we employ inflation for one of the annuli so that the inversion symmetry is broken, while C3 symmetry is preserved. Inflating the lower annulus leads to A-type unit cells, as shown in Fig. 2(c), while inflating the upper annulus leads to B-type unit cells as shown in Fig. 2(d). The inflation results in the gap opening as illustrated in Fig. 3(b).

The benefit of using large deformations to tune the bandgap at the K point via different stretch values ξ for different material models is shown in Fig. 4(b). We denote $\Delta r = r_0^{\text{lower}} - r_0^{\text{upper}}$ as the difference in the inner radius between the lower and upper annulus, r_0^{lower} and r_0^{upper}, respectively. The radii are dependent on the stretch ξ and are computed as in Eq. (4). Figure 4(b) shows the eigenfrequencies and the band gap width of the first two eigenmodes using the three different hyperelastic models as well as a linear elastic material model. Figure 4(b) shows that the larger stretch induces stronger SIS breaking, hence a larger bandgap width. Furthermore, for both hyperelastic and linear elastic material models, the bandgap width increases nonlinearly with increasing Δr, with little difference observed between the three hyperelastic

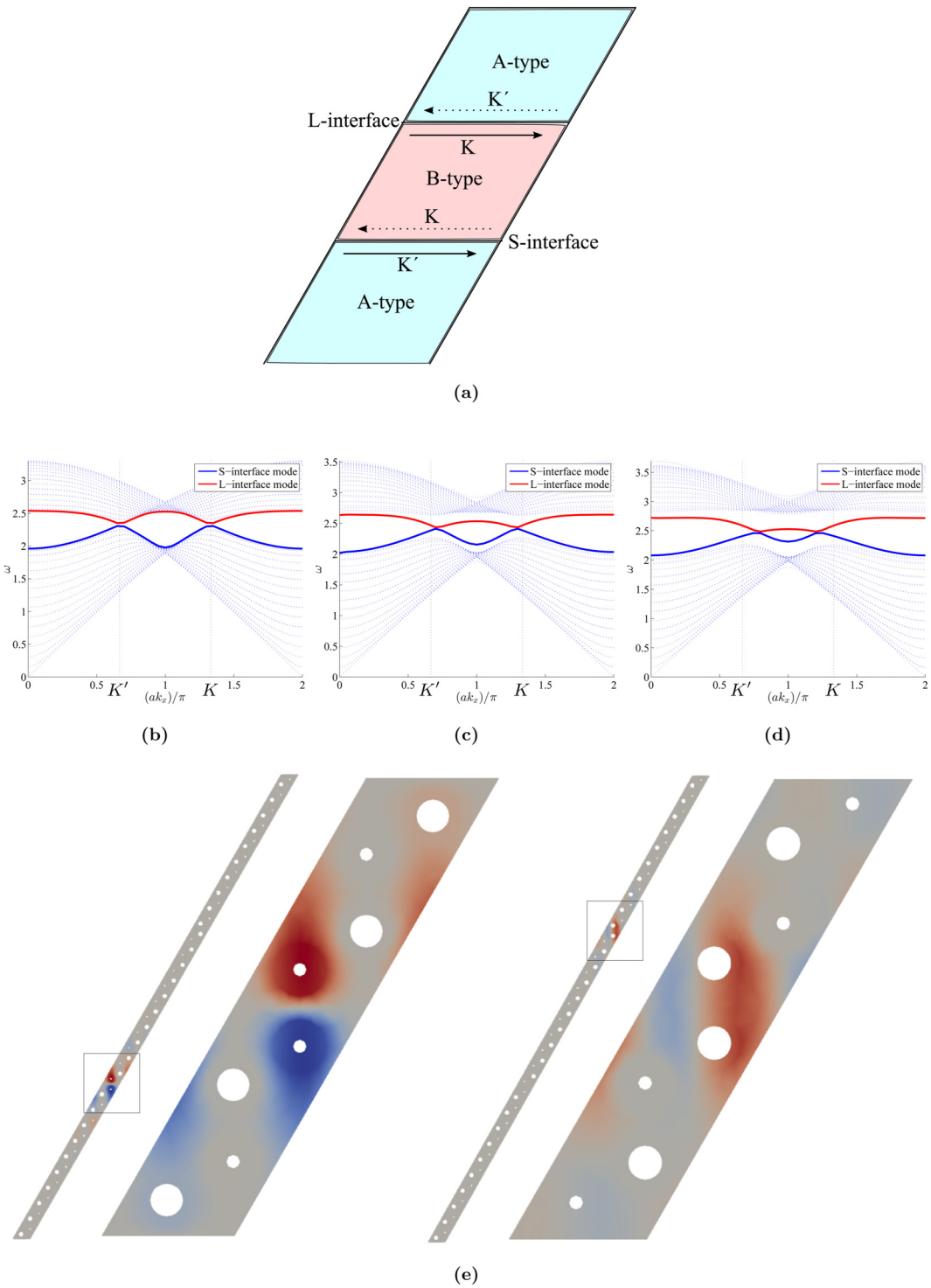

FIG. 7. Domain wall edge state. (a) Schematic view of a finite cell consists of two interfaces, S- and L-interface. (b)–(d) Phononic band structure of a finite strip with $\xi = 1.1,\ 1.5$, and 2.0, respectively. S- and L-interface modes appear in the bandgap. (e) Anti-symmetric eigenmode of the S-interface (left) and the symmetric eigenmode of the L-interface (right).

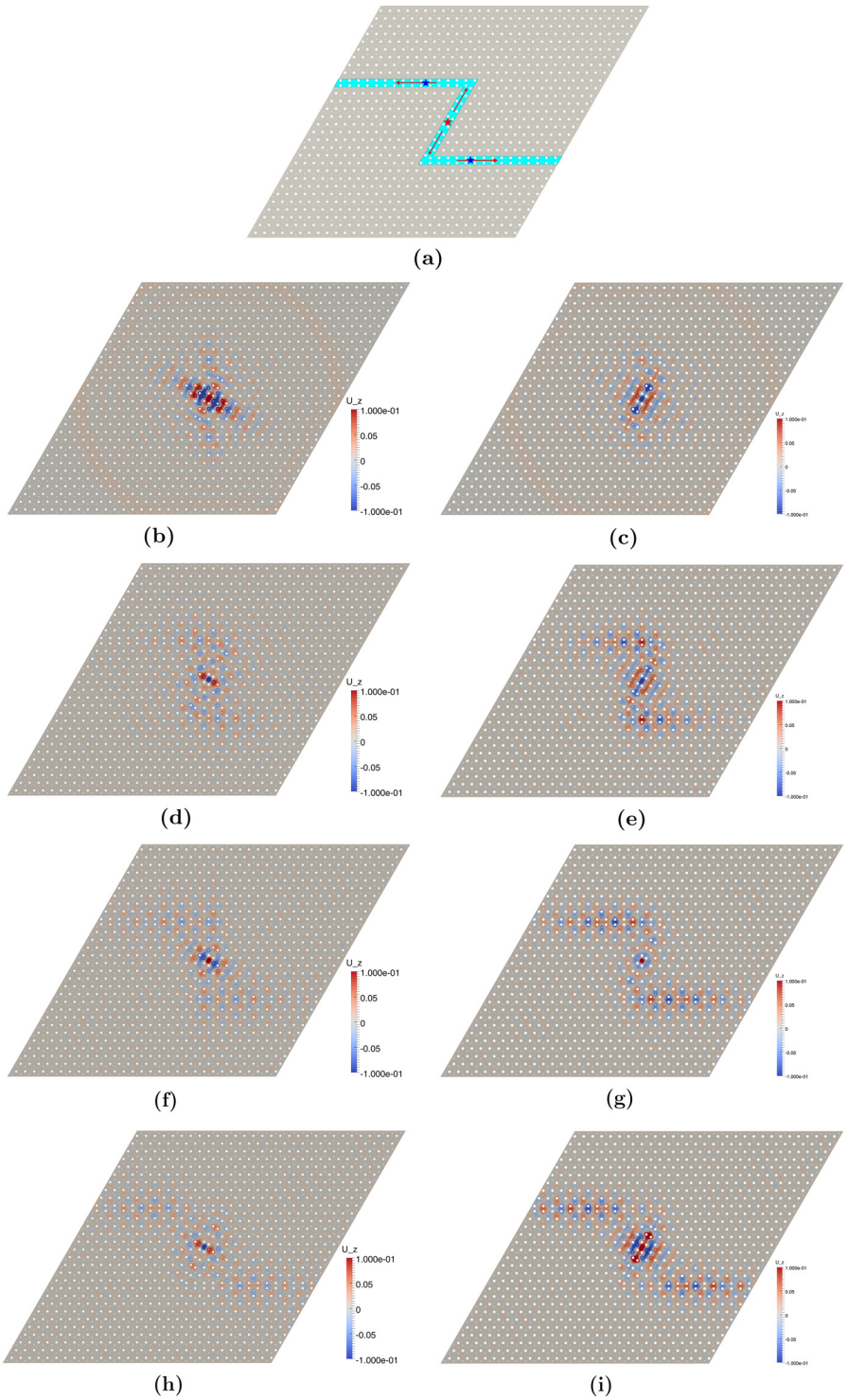

FIG. 8. Edge-mode propagation in the L-interface in two cases, $\xi = 1.5$ (left column) and $\xi = 2.0$ (right column). (a) The phononic crystal is excited harmonically at the center (red star). Two reference points are at point A and B (upper and lower blue stars, respectively).

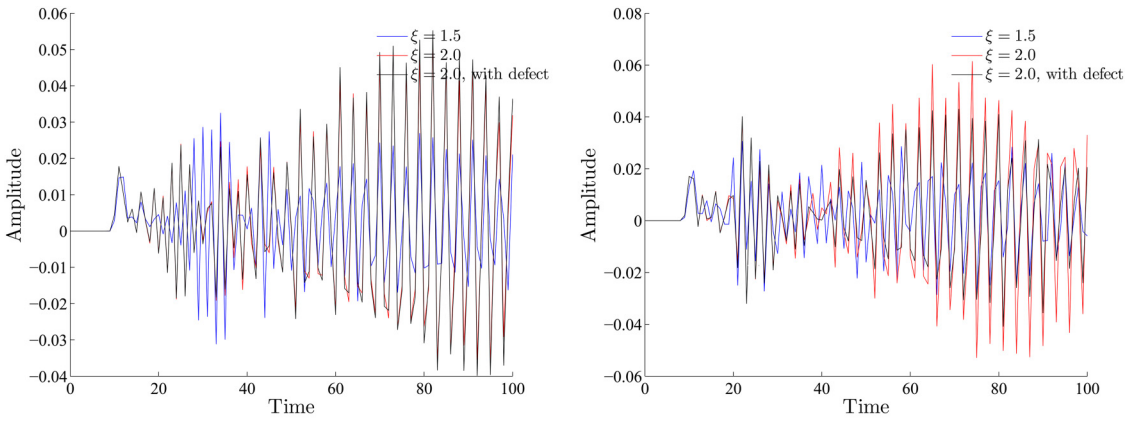

(a) Time history of displacement at point A (b) Time history of displacement at point B

FIG. 9. Time history of displacement at points of interest along the topologically non-trivial interface with different stretch values.

models and the linear elastic model. Because of this, the Neo-Hookean model will be chosen for the rest of the paper.

It is also interesting that the linear and nonlinear material models lead to effectively the same bandgap widths with increasing Δr, which suggests that large geometric changes, rather than material nonlinearity, are key to shifting the bandgap. This is expected from the current mechanism, since the pre-stress only induces anisotropic behavior inside the annulus with the tangent elastic moduli given by Eq. (10).[24] The components of the tangent elastic moduli are dependent on the incremental shear moduli given in Eq. (7), whose variations in the radial direction can be found in the Appendix. Specifically, for the case when $\xi = 1.5$, as shown in Fig. 11, there are spatial variations in the incremental shear moduli as compared to the initial shear modulus of the annulus μ_1. Consequently, the variation of the tangent elastic moduli inside the annulus is demonstrated in Fig. 12 showing the anisotropic behavior of the pre-stressed annular. Note that there are both increases and decreases in the elastic moduli, which result in minor changes to the bandstructure, illustrating the weak effect of material nonlinearity for this particular situation. Because we employ small amplitude excitations, i.e., a linear wave with small amplitude rather than large amplitude, which could induce a nonlinear wave due to geometric nonlinearities, on the current configuration, we do not account for geometric nonlinearities, which may also impact the bandstructure. More importantly, although the eigenfrequencies are the same for both lattices with respect to the same stretch, their eigenmodes are flipped as shown in the insets of Fig. 4(a). The inversion of the eigenmodes indicates that the phase transition has taken place at the undeformed unit cell, i.e., $\Delta r = 0$.

We further investigate the topological phase transition by computing the Berry curvature of the first two eigenmodes of both unit cells A and B. The Berry curvature for the eigenmode nth at the wave vector $\mathbf{k}$ is given as

$$B^n(k) = -2\mathrm{Im}\sum_{n\neq m}\frac{\langle \Phi_m \mid \frac{\partial \mathbf{K}}{\partial k_x} \mid \Phi_n\rangle\langle \Phi_n \mid \frac{\partial \mathbf{K}}{\partial k_y} \mid \Phi_m\rangle}{\left(\omega_m^2 - \omega_n^2\right)^2}, \tag{12}$$

where Φ_m and Φ_n are the mth and nth eigenvectors, respectively. The Berry curvature of the first two eigenmodes of both unit cells subjected to stretch $\xi = 1.5$ is presented in Fig. 5. The Berry curvature is localized at the K and K′ points and carries different signs at these points. Consequently, the integral over the first Brillouin zone of the Berry curvature, which defines the topological invariant known as the Chern number $C^n = \frac{1}{2\pi}\int_{BZ} B^n(\mathbf{k})\mathrm{d}^2\mathbf{k}$, is null. This is expected in a system where the time reversal symmetry is intact. Nevertheless, since the Berry curvature is sharply centered around the Dirac points, the integration over a small region bounded around the valley characterizes the topological charge, also known as the valley Chern number

$$C_v^n = \frac{1}{2\pi}\int_v B^n(\mathbf{k})\mathrm{d}^2\mathbf{k}. \tag{13}$$

By using the $\mathbf{k}\cdot\mathbf{p}$ theory, the valley Chern number can be analytically computed. For lattice A, the lower (upper) mode carries $C_v^1 = -1/2(1/2)$ and $C_v^1 = 1/2(-1/2)$ at K and K′ valleys, respectively, whereas for lattice B, these topological invariants are inverted. As a result, when an interface is formed between these two lattices, the difference in the contrasted valley Chern number, e.g., $\left|C_{v,K}^{1,A} - C_{v,K}^{1,B}\right| = 1$ indicates the number of edge or interface mode in such structures according to the bulk-edge correspondence.[27]

However, our numerical integration of Eq. (13) over a small square region around the Dirac points gives the value ± 0.3. This deviation as compared to the analytical result may

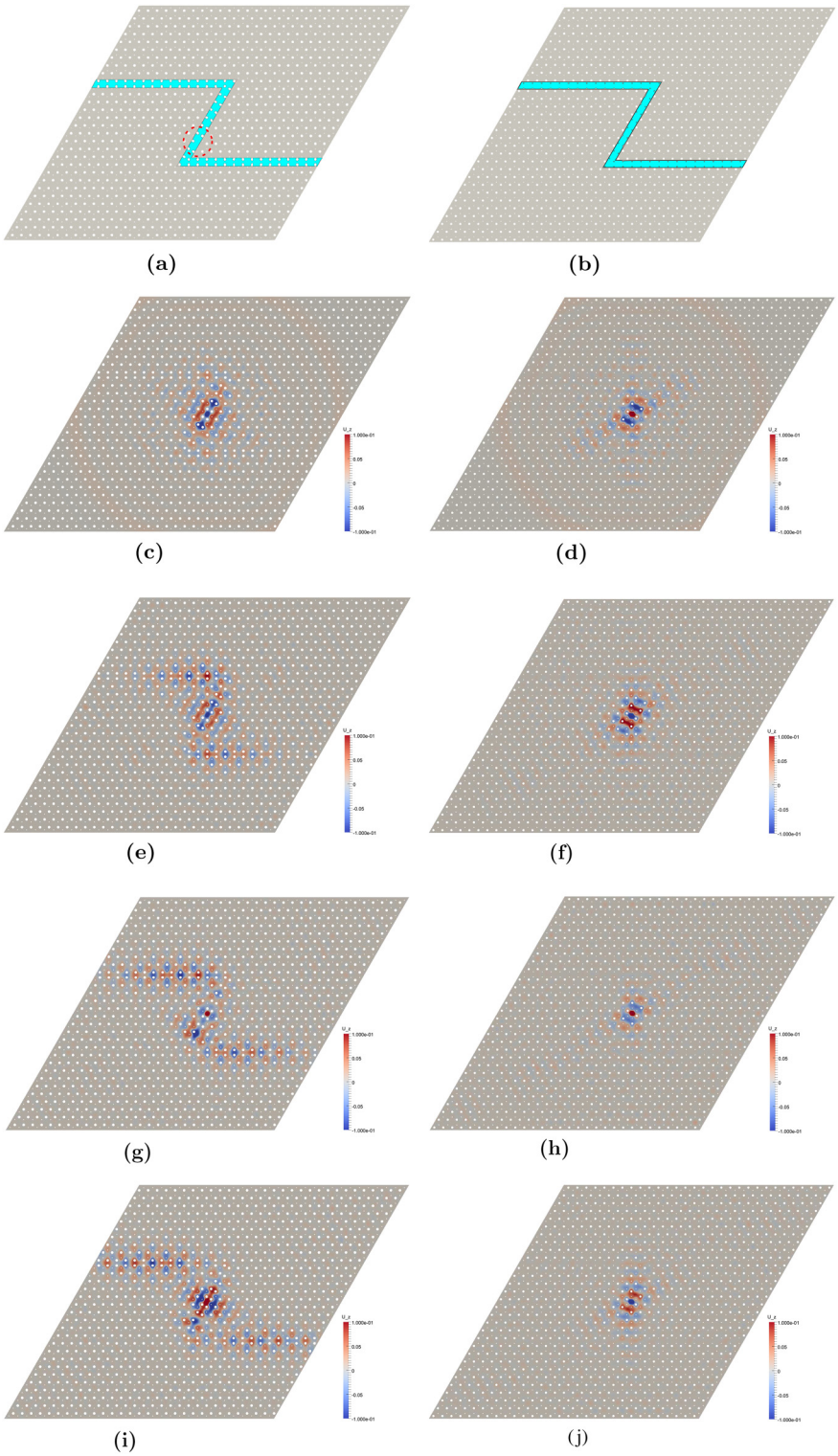

FIG. 10. Edge-mode propagation along the L-interface with the defect (left column), along the S-interface (right column).

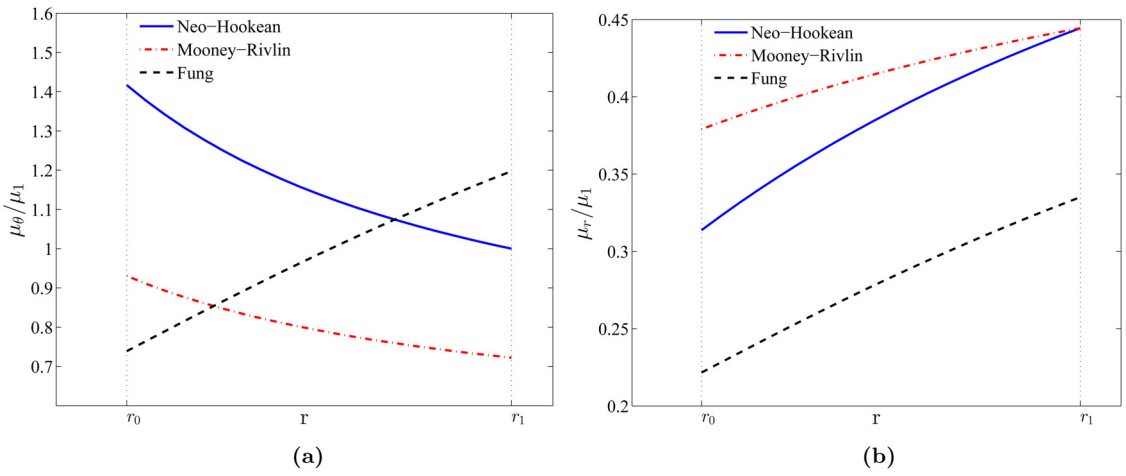

FIG. 11. Variation of incremental shear moduli in the radial direction when $\xi = 1.5$. The results are normalized with respect to the initial shear modulus of the annular μ_1.

be caused by the strong SIS breaking.[10] In fact, the smaller the stretch ξ, i.e., the weaker the SIS breaking, the Berry curvature is more localized at K and K' points, and the valley Chern number approaches ± 0.5 as shown in Fig. 6.

III. VALLEY HALL EDGE STATE

The existence of the interface mode is revealed by studying the dispersion of a finite super cell, which has an interface between A and B lattices. The super cell consists of 10 B-type unit cells placed in between 20 A-type unit cells, which then forms two types of interfaces, namely, "small" (S) and "large" (L) denoting when the A-type unit cell is on top of the B-type unit cell and vice versa, respectively, as shown in Fig. 7(a). The periodic boundary condition is applied on the left and right edges of the super cell. Subsequently, the dispersion relation can be obtained by solving the eigenvalue problem. As expected from the bulk-edge correspondence, a pair of interface modes emerges within the bandgap, corresponding to the S- and L-interface as shown in Figs. 7(b)–7(d), which show the energy band diagram along k_x with stretch $\xi = 1.1$, 1.5, and 2.0, respectively. Here, we remark that, for a small stretch value, e.g., $\xi = 1.1$, although the SIS is broken and a bandgap is opened, the interface mode cannot be detached from the bulk mode [see Fig. 7(b)]. On the other hand, the interface mode can be seen distinctly from the bulk with a large stretch value as in Fig. 7(d).

In those figures, the two vertical dashed lines mark the projection of two valley points K and K' on the interface, such that at the K' point, the S-interface and L-interface support forward and backward propagating waves, respectively, whereas the opposite observation can be deduced for the K point due to the TRS. As a result, the difference in the momentum space between the forward and backward propagating waves ensures these edge states are essentially immune to backscattering.[10] Furthermore, we show the eigenmodes of the S- and L-interface calculated at $k_x = \pi/a$ with $\xi = 1.5$ in Fig. 7(e). The displacement amplitude is localized at the interface. More noticeably, the eigenmodes of the S- and L-interface are antisymmetric and symmetric, respectively, with respect to the interface. Although both types of interface have equivalent topological order $C_v = \pm 1$, the symmetric eigenstate is coupled well with the incident wave, whereas the anti-symmetric eigenstate suppresses it.[10,15] This phenomenon will be observed in Sec. IV.

IV. EDGE STATE WAVE PROPAGATION

In this section, we will verify the one-way wave propagation in an interface formed by A-type and B-type unit cells through direct numerical simulation. A structure of 30×30 unit cells, which can have either S- or L-interface zig-zag paths [see Figs. 8(a) and 10(b)], is harmonically excited at the center [the red star in Fig. 8(a)] with angular frequency $\omega = 2.6$ (which lies within the topologically-protected bandgap frequency) as schematically shown in Fig. 8(a). During the transient FEM simulation, an absorbing boundary condition is applied to the four outer edges to mimic an infinite structure and to prevent the wave reflection from the boundaries. Specifically, we investigate the performance of the edge-mode propagation for different stretch values ξ, for both L and S interfaces, and also with the existence of defects along the interface.

Figure 8 presents the wave propagation for the L-interface with two different stretch values $\xi = 1.5$ (left column) and $\xi = 2.0$ (right column). In both cases, the symmetric eigenstate is excited and the displacement is localized and propagated along the L-interface. However, the structure with $\xi = 2$ can prevent waves from penetrating into the bulk due to the bigger bandgap as compared to that in the case $\xi = 1.5$ [Figs. 7(c) and 7(d)]. For a closer look, Fig. 9 shows the time history of displacements at two

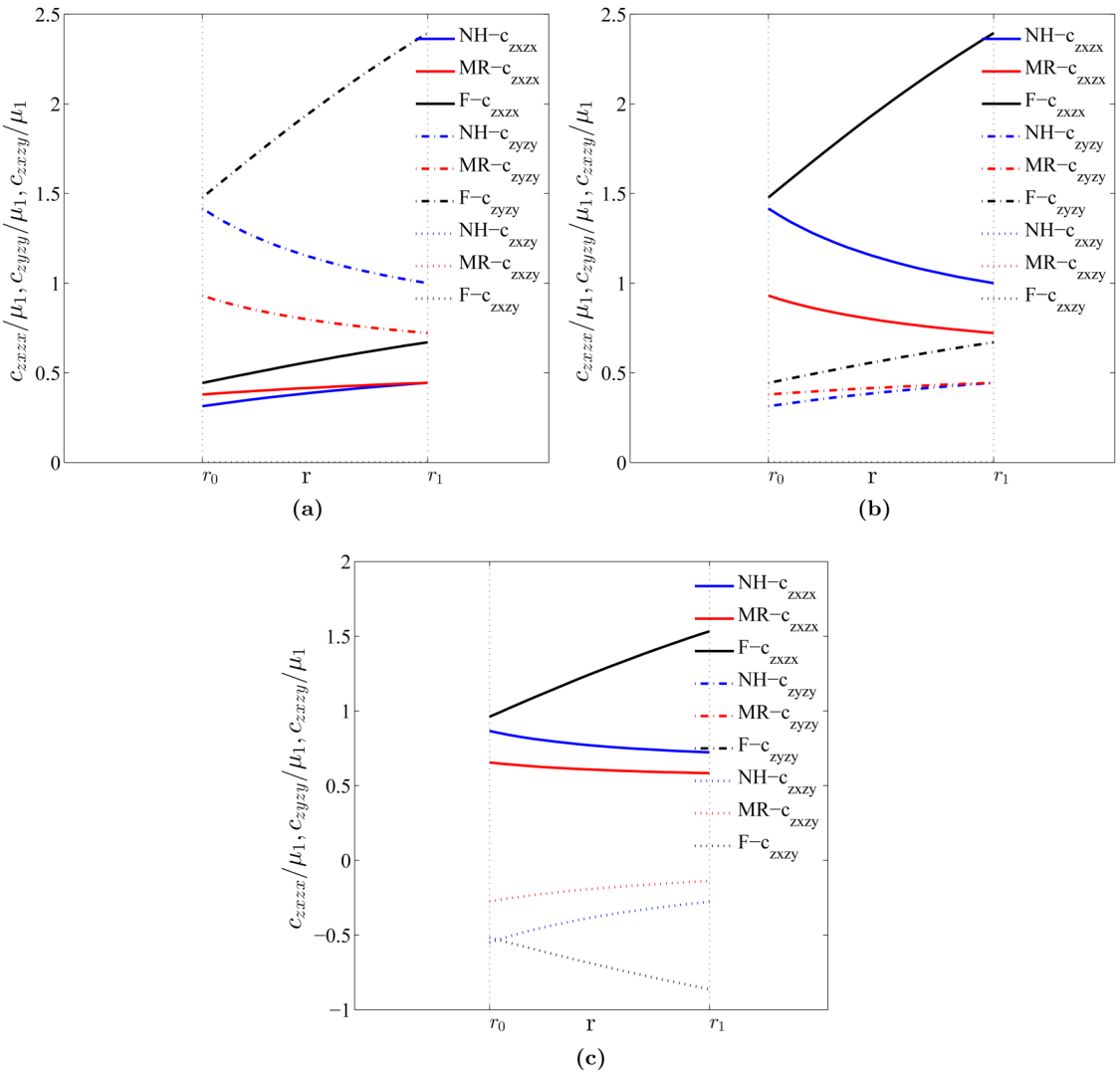

FIG. 12. Variation of the elastic moduli. The results are normalized with respect to the initial shear modulus of the annulus μ_1. (a) Variation of elastic moduli as $y = 0$, $r_0 < x < r_1$. Component c_{zxzx} decreases, but c_{zyzy} increases. The shear components are reduced. (b) Variation of elastic moduli as $x = 0$, $r_0 < y < r_1$. Component c_{zyzy} decreases but c_{zxzx} increases. The shear components are reduced. (c) Variation of elastic moduli as $r_0 < x = y < r_1$.

reference points A and B along the interface [the upper and lower blue stars, respectively, in Fig. 8(a)], calculated from the same excitation source. The amplitude in the case $\xi = 1.5$ is smaller than when $\xi = 2.0$, indicating that more of the input energy is confined to the interface as the stretch increases. We note that while the valley Chern number C_v when $\xi = 1.5$ is closer to the theoretical value than when $\xi = 2.0$, which seems to suggest that deviations from the theoretical valley Chern number do not deleteriously affect the performance of the topologically-protected interface and may enable enhanced energy localization due to the larger bandgap that can result.

In addition, we study the wave propagation along a topologically non-trivial interface that contains a defect, which is created by removing an annulus inside the red dashed circle in Fig. 10(a). As expected from the robust backscattering immunity of the interface mode, the displacement is again localized and travels along the L-interface. On the other hand, the edge state of the S-interface is suppressed by the antisymmetric eigenstate such that the displacement is only localized at the source as can be seen in Figs. 10(d), 10(f), 10(h), and 10(j). We also remark that in terms of time history displacement, at point A, the amplitude of the displacement is not altered with and without the defect in the L-interface

[Fig. 9(a)]. Meanwhile, the amplitude at point B is slightly reduced as compared to the perfect one since the defect lies on the wave propagation path [Fig. 9(a)].

V. CONCLUSIONS

We have proposed a tunable quantum valley Hall phononic topological insulator that is based on a strain-driven mechanism, in which the occurrence of the topological phase transition is induced by alternatively inflating a soft inclusion embedded in an elastic host medium. While the utilization of a soft material is beneficial in the ability to generate large deformations for relatively low stresses, material nonlinearities generated due to the large deformation do not appear to significantly affect the resulting width or frequency of the topological bandgap. Within our formulation, which considers small perturbations about a largely deformed state, the effects of geometric nonlinearity, which may also impact the bandgap, are not considered, which will be a focus of future work. The intensity of the SIS breaking can be mechanically modulated by the internal pressure or axial stretch, which enables tunable topological properties, in particular, control over the bandgap width as well as the frequency at which the topologically protected phonons can propagate. Numerical simulations served to demonstrate the robustness of the protected interface phonons, where defects such as sharp bends and geometric imperfections did not impact the propagation of the interface phonons. While the specific geometry considered in this work has not been studied experimentally with regard to topologically-protected wave propagation, we note that recent experimental studies have demonstrated the possibility of achieving topologically-protected wave propagation using soft, hyperelastic materials similar to the ones considered in the present work. Thus, the current study can be a guide for designing strain-tunable topological soft phononic crystals.

ACKNOWLEDGMENTS

B. H. Nguyen and X. Zhuang owe gratitude to the sponsorship from the Sofja Kovalevskaja Programme of Alexander von Humboldt Foundation. H.S.P. acknowledges the support of the Army Research Office (ARO) (Grant No. W911NF-18-1-0380).

APPENDIX A: MATERIAL MODEL

In this section, we summarize three incompressible material models for the soft annulus. For the Mooney-Rivlin material, the energy density function is given as[23]

$$W = \frac{\mu}{2}\left[s_1\left(\lambda_r^2+\lambda_\theta^2+\lambda_z\right)+\left(1-s_1^2\right)\left(\lambda_r^2\lambda_\theta^2+\lambda_r^2\lambda_z^2+\lambda_\theta^2\lambda_z^2-3\right)\right], \quad \text{(A1)}$$

where $s_1 \in [0, 1]$ is a material constant. When $s_1 = 1$, the above function corresponds to the energy density function of the Neo-Hookean material. We note that in our numerical results, the value s_1 is chosen to be 0.5. Substituting Eq. (A1) into Eq. (7), the incremental shear moduli can be obtained as[23]

$$\mu_r(r) = \frac{T\mu_1}{\xi^2}\left(1+\frac{m}{r^2}\right), \qquad \text{for } r_0 < r < r_1, \quad \text{(A2a)}$$

$$\mu_\theta(r) = \frac{T\mu_1}{\xi^2}\left(1-\frac{m}{r^2+M}\right), \qquad \text{for } r_0 < r < r_1, \quad \text{(A2b)}$$

with $M = (1/\xi - 1)R_1^2$, $T = 1 + (\xi - 1)s_1$, $m = \frac{M\xi s_1}{T}$. We also considered a simplified version of the Fung material, which has the energy density function

$$W = \frac{\mu_1}{2}[\exp(Q) - 1], \quad \text{(A3)}$$

where $Q = \frac{1}{2}(\lambda_r^2 + \lambda_\theta^2 + \lambda_z^2 - 3)$. Similarly, the incremental shear moduli can be derived from Eq. (7),

$$\mu_r(r) = \frac{\mu_1(r^2+M)}{2\xi r^2}\left(\frac{r^2+M}{\xi r^2}+\xi-1\right), \quad \text{(A4a)}$$

$$\mu_r(r) = \frac{\mu_1\xi(r^2+M)}{2r^2}\left(\frac{(r^2+M)\xi}{r^2}+\xi-1\right). \quad \text{(A4b)}$$

The variation of the incremental shear moduli when $\xi = 1.5$ is demonstrated in Fig. 11. Consequently, the elastic moduli can be computed from these incremental shear moduli from Eq. (10). As a demonstrative example, let us consider an annulus schematically depicted in Fig. 1 that takes the center as the origin of the Cartesian coordinate system. The variation of the elastic moduli in three cases is shown in Fig. 12.

APPENDIX B: DISCRETIZATION

In this section, we present the matrix form of the finite element discretization. Using the bilinear 4-node quadrilateral element, the out-of-plane displacement w is approximated from the nodal displacement $\hat{\mathbf{w}} = [w_1 \;\; w_2 \;\; w_3 \;\; w_4]^T$ and the basis functions $\mathbf{N} = [N_1 \;\; N_2 \;\; N_3 \;\; N_4]$, such that $w = \mathbf{N}\hat{\mathbf{w}}$. Consequently, the displacement gradient ∇w can be approximated by $\nabla w = \mathbf{B}\mathbf{w}$, where the differential operator $\mathbf{B}$ is given as

$$\mathbf{B} = \begin{bmatrix} \frac{\partial N_1}{\partial x} & \frac{\partial N_2}{\partial x} & \frac{\partial N_3}{\partial x} & \frac{\partial N_4}{\partial x} \\ \frac{\partial N_1}{\partial y} & \frac{\partial N_2}{\partial y} & \frac{\partial N_3}{\partial y} & \frac{\partial N_4}{\partial y} \end{bmatrix}. \quad \text{(B1)}$$

Bloch's theorem is applied such that

$$w(\mathbf{x}) = \tilde{w}(\mathbf{x})\exp(i\omega t - i\mathbf{k}\cdot\mathbf{x}), \quad \text{(B2)}$$

where $\tilde{w}(\mathbf{x})$ is the periodic function with the same periodicity with the crystal. The above relation can be expressed in terms of nodal values as

$$\hat{\mathbf{w}} = \exp(i\omega t)\mathbf{T}\tilde{\mathbf{w}}, \quad \text{(B3)}$$

where $\hat{\mathbf{w}} = [\hat{w}_1 \quad \hat{w}_2 \quad \hat{w}_3 \quad \hat{w}_4]^T$ and

$$\mathbf{T} = \begin{bmatrix} \exp(i\mathbf{k}\cdot\mathbf{x}_1) & 0 & 0 & 0 \\ 0 & \exp(i\mathbf{k}\cdot\mathbf{x}_2) & 0 & 0 \\ 0 & 0 & \exp(i\mathbf{k}\cdot\mathbf{x}_3) & 0 \\ 0 & 0 & 0 & \exp(i\mathbf{k}\cdot\mathbf{x}_4) \end{bmatrix}. \tag{B4}$$

Upon multiplying Eq. (8) with the test function δw and employing integration by parts, the stiffness and mass matrices can be obtained as

$$\bar{\mathbf{K}} = \bigcup_{e=1}^{nel} \bar{\mathbf{k}}^e = \bigcup_{e=1}^{nel} \int_{\Omega^e} \mathbf{B}^T \mathbf{C}\, \mathbf{B} d\Omega, \tag{B5a}$$

$$\bar{\mathbf{M}} = \bigcup_{e=1}^{nel} \bar{\mathbf{m}}^e = \bigcup_{e=1}^{nel} \int_{\Omega^e} \rho\, \mathbf{N}^T \mathbf{N} d\Omega, \tag{B5b}$$

where $\mathbf{C}(x,y) = \begin{bmatrix} C_{zxzx}(x,y) & C_{zxzy}(x,y) \\ C_{zxzy}(x,y) & C_{zyzy}(x,y) \end{bmatrix}$, whose components are computed from Eq. (10). Thus, the eigenvalue problem can be re-written as

$$\bigcup_{e=1}^{nel} \bar{\mathbf{k}}^e \mathbf{T}\hat{\mathbf{w}} = \bigcup_{e=1}^{nel} \omega^2 \bar{\mathbf{m}}^e \mathbf{T}\hat{\mathbf{w}}. \tag{B6}$$

By pre-multiplying the above equation with $\mathbf{T}^*$, the complex conjugate of $\mathbf{T}$, one can obtain the equivalent eigenvalue problem with Hermitian positive definite matrices

$$\mathbf{K}\hat{\mathbf{w}} = \omega^2 \mathbf{M}\hat{\mathbf{w}}, \tag{B7}$$

with

$$\mathbf{K} = \bigcup_{e=1}^{nel} \mathbf{T}^* \bar{\mathbf{k}}^e \mathbf{T}, \tag{B8a}$$

$$\mathbf{M} = \bigcup_{e=1}^{nel} \mathbf{T}^* \bar{\mathbf{m}}^e \mathbf{T}. \tag{B8b}$$

Further details about the numerical implementation can also be found in Ref. 28.

REFERENCES

[1]M. Z. Hasan and C. L. Kane, "Colloquium: Topological insulators," Rev. Mod. Phys. **82**, 3045 (2010).
[2]L. M. Nash, D. Kleckner, A. Read, V. Vitelli, A. M. Turner, and W. T. Irvine, "Topological mechanics of gyroscopic metamaterials," Proc. Natl. Acad. Sci. **112**, 14495–14500 (2015).
[3]P. Wang, L. Lu, and K. Bertoldi, "Topological phononic crystals with one-way elastic edge waves," Phys. Rev. Lett. **115**, 104302 (2015).
[4]Z. Yang, F. Gao, X. Shi, X. Lin, Z. Gao, Y. Chong, and B. Zhang, "Topological acoustics," Phys. Rev. Lett. **114**, 114301 (2015).
[5]S. H. Mousavi, A. B. Khanikaev, and Z. Wang, "Topologically protected elastic waves in phononic metamaterials," Nat. Commun. **6**, 8682 (2015).
[6]R. Süsstrunk and S. D. Huber, "Observation of phononic helical edge states in a mechanical topological insulator," Science **349**, 47–50 (2015).
[7]R. K. Pal, M. Schaeffer, and M. Ruzzene, "Helical edge states and topological phase transitions in phononic systems using bi-layered lattices," J. Appl. Phys. **119**, 084305 (2016).
[8]C. He, X. Ni, H. Ge, X.-C. Sun, Y.-B. Chen, M.-H. Lu, X.-P. Liu, and Y.-F. Chen, "Acoustic topological insulator and robust one-way sound transport," Nat. Phys. **12**, 1124 (2016).
[9]J. Vila, R. K. Pal, and M. Ruzzene, "Observation of topological valley modes in an elastic hexagonal lattice," Phys. Rev. B **96**, 134307 (2017).
[10]H. Zhu, T.-W. Liu, and F. Semperlotti, "Design and experimental observation of valley-hall edge states in diatomic-graphene-like elastic waveguides," Phys. Rev. B **97**, 174301 (2018).
[11]J.-J. Chen, S.-Y. Huo, Z.-G. Geng, H.-B. Huang, and X.-F. Zhu, "Topological valley transport of plate-mode waves in a homogenous thin plate with periodic stubbed surface," AIP Adv. **7**, 115215 (2017).
[12]L. Yang, K. Yu, Y. Wu, R. Zhao, and S. Liu, "Topological edge states for flexural waves in perforated phononic plates," J. Phys. D: Appl. Phys. **51**, 325302 (2018).
[13]J. Li, J. Wang, S. Wu, and J. Mei, "Pseudospins and topological edge states in elastic shear waves," AIP Adv. **7**, 125030 (2017).
[14]X. Wen, C. Qiu, J. Lu, H. He, M. Ke, and Z. Liu, "Acoustic dirac degeneracy and topological phase transitions realized by rotating scatterers," J. Appl. Phys. **123**, 091703 (2018).
[15]J. Lu, C. Qiu, L. Ye, X. Fan, M. Ke, F. Zhang, and Z. Liu, "Observation of topological valley transport of sound in sonic crystals," Nat. Phys. **13**, 369 (2017).
[16]R. K. Pal and M. Ruzzene, "Edge waves in plates with resonators: An elastic analogue of the quantum valley hall effect," New J. Phys. **19**, 025001 (2017).
[17]T.-W. Liu and F. Semperlotti, "Tunable acoustic valley-Hall edge states in reconfigurable phononic elastic waveguides," Phys. Rev. Appl. **9**, 014001 (2018).
[18]R. Chaunsali, C.-W. Chen, and J. Yang, "Experimental demonstration of topological waveguiding in elastic plates with local resonators," New J. Phys. **20**, 113036 (2018).
[19]J.-W. Jiang, B.-S. Wang, and H. S. Park, "Topologically protected interface phonons in two-dimensional nanomaterials: Hexagonal boron nitride and silicon carbide," Nanoscale **10**, 13913–13923 (2018).
[20]T.-W. Liu and F. Semperlotti, "Experimental evidence of robust acoustic valley Hall edge states in a topological elastic waveguide," Phys. Rev. Applied **11**, 014040 (2019).
[21]R. Susstrunk, P. Zimmermann, and S. D. Huber, "Switchable topological phonon channels," New J. Phys. **19**, 015013 (2017).
[22]E. Barnwell, "One and two-dimensional propagation of waves in periodic heterogeneous media: Transient effects and band-gap tuning," Ph.D. thesis (University of Manchester, 2015).
[23]E. G. Barnwell, W. J. Parnell, and I. D. Abrahams, "Antiplane elastic wave propagation in pre-stressed periodic structures; tuning, band gap switching and invariance," Wave Motion **63**, 98–110 (2016).
[24]W. J. Parnell, "Nonlinear pre-stress for cloaking from antiplane elastic waves," Proc. R. Soc. A **468**, 563–580 (2011).
[25]M. Destrade, "Incremental equations for soft fibrous materials," in *Nonlinear Mechanics of Soft Fibrous Materials* (Springer, 2015), pp. 233–267.
[26]R. W. Ogden, "Incremental statics and dynamics of pre-stressed elastic materials," in *Waves in Nonlinear Pre-stressed Materials* (Springer, 2007), pp. 1–26.
[27]W. Yao, S. A. Yang, and Q. Niu, "Edge states in graphene: From gapped flat-band to gapless chiral modes," Phys. Rev. Lett. **102**, 096801 (2009).
[28]L. Han, Y. Zhang, X.-m. Li, L.-h. Jiang, and D. Chen, "Accelerated approach for the band structures calculation of phononic crystals by finite element method," Crystals **6**, 11 (2016).